Applied Physics A (2026) 132:441
https://doi.org/10.1007/s00339-026-09622-y

Applied Physics A
Materials Science & Processing

Rapid thermal annealing of CIGS thin film as an absorber layer without external selenization

Ghadeer Albalawneh[1] · Muhammad Mahyiddin Ramli[1,2] · Mohd Zamzuri Mohammad Zain[3] · Zaliman Sauli[2] · Nurul Huda Osman[4] · Ali H. Reshak[5,6]

Received: 10 December 2025 / Accepted: 15 April 2026 / Published online: 23 April 2026

Abstract
Copper indium gallium diselenide (Cu(In, Ga)Se_2, CIGS) is a promising absorber material for thin-film photovoltaic applications owing to its tunable bandgap and high optical absorption coefficient. However, conventional fabrication of CIGS solar cells typically relies on vacuum-based deposition techniques followed by high-temperature selenization processes, which increase manufacturing cost, process complexity, and environmental concerns. In this study, a solution-based fabrication method that eliminates the need for conventional post-selenization is investigated by introducing intermediate spin-coated selenium (Se) ink layers within CIGS precursor films. The influence of inserting different numbers of Se interlayers (0, 3, and 7 spin-coating cycles) between CIGS precursor layers on film morphology, crystallinity, composition, and device performance was systematically examined. SEM and EDX analyses revealed increased grain size, improved film densification, and enhanced selenium incorporation with increasing numbers of Se interlayers. X-ray diffraction results confirmed improved crystallinity and phase purity, while optical measurements showed a gradual bandgap reduction from 1.238 eV to 1.203 eV with increasing selenium incorporation. The best-performing device (7Se/8CIGS) achieved a power conversion efficiency of 5.13%, which is significantly higher than that of the selenium-free device (3.15%). These results demonstrate that controlled selenium incorporation through spin-coated Se interlayers significantly enhances the structural quality and optoelectronic properties of solution-processed CIGS absorber layers. The proposed strategy provides a scalable and environmentally friendly route for fabricating CIGS thin-film solar cells without hazardous gas-phase selenization processes.

Keywords CIGS solar cells · Solution-processed photovoltaics · Selenization-free fabrication · Thiol-amine solvents · Thin-film solar technology

✉ Muhammad Mahyiddin Ramli
mmahyiddin@unimap.edu.my

[1] Institute of Nano Electronic Engineering (INEE), Universiti Malaysia Perlis (UniMAP), 02600 Arau, Perlis, Malaysia

[2] Faculty of Electronic Engineering & Technology, Universiti Malaysia Perlis (UniMAP), 02600 Arau, Perlis, Malaysia

[3] Faculty of Mechanical Engineering & Technology, Universiti Malaysia Perlis (UniMAP), 02600 Arau, Perlis, Malaysia

[4] Applied Electromagnetic Laboratory 1, Department of Physics, Faculty of Science, Universiti Putra Malaysia, 43400 UPM Serdang, Selangor, Malaysia

[5] Physics Department, College of Science, University of Basrah, Basrah 61004, Iraq

[6] Department of Instrumentation and Control Engineering, Faculty of Mechanical Engineering, Czech Technical University in Prague, Technicka 4, 166 07 Prague 6, Czech Republic

1 Introduction

Copper indium gallium diselenide (Cu(In, Ga)Se_2, or CIGS) is regarded as a leading absorber material for thin-film photovoltaic applications due to its high optical absorption coefficient (~ 10^5 cm^{-1}), direct band gap, exceptional defect tolerance, and tunable band gap (1.04–1.68 eV), which enables effective spectral matching with solar radiation [1–3]. The laboratory efficiency of CIGS solar cells is comparable to that of crystalline silicon solar cells. However, silicon technology currently dominates the commercial photovoltaic market due to its mature manufacturing infrastructure and large-scale production. The current world-record efficiency for CIGS solar cells is 23.6% [4], which is comparable to the efficiency of crystalline silicon solar cells under laboratory conditions. However, crystalline silicon remains

the dominant technology in the commercial photovoltaic market due to its mature manufacturing infrastructure and large-scale industrial deployment. Most high-performance CIGS solar cells have been fabricated using vacuum-based deposition methods such as co-evaporation [5–7] and one-step sputtering [8, 9]. However, vacuum-based fabrication processes require sophisticated equipment and precise process control, which increases manufacturing complexity and cost and can make large-area production more challenging. A two-step process involving the deposition of a precursor followed by high-temperature selenization has garnered considerable attention as an alternative method for absorber formation. This approach has been highlighted for its potential to achieve high conversion efficiency while maintaining low costs and improving productivity [10–12]. Solar Frontier has recently demonstrated the potential for high efficiency through a two-step process, achieving an efficiency of 19.2% for an 841 cm^2 CIGS sub-module, by using a sputtering method to create the metallic precursor films [13]. Moreover, non-vacuum solution-based deposition methods significantly improve the cost-effectiveness of the fabrication process [14, 15]. In recent years, solution-processed fabrication approaches have attracted significant attention for large-area photovoltaic manufacturing due to their compatibility with low-cost deposition techniques such as spin coating, printing, and roll-to-roll processing. These approaches have been widely explored in emerging photovoltaic technologies, including perovskite solar cells, where solution-based processing has enabled rapid improvements in device efficiency and scalability. Similar concepts are increasingly being investigated for chalcopyrite absorbers such as CIGS, where solution-based deposition offers a promising route to reduce fabrication complexity while maintaining good material quality. In this context, numerous combinations of non-vacuum deposition techniques and precursor materials for the formation of CIGS thin films have been thoroughly examined [16–19].

Solution-based processing is considered a highly viable approach for the commercialization of large-area solar cells due to its potential to significantly reduce solar electricity costs [14, 15]. This method typically involves a two-step process: initially, a uniform precursor solution is deposited at room temperature using techniques such as spin coating, spray coating, or inkjet printing. Subsequently, the film undergoes selenization through thermal annealing at temperatures between 450 °C and 600 °C, enabling the conversion of the precursor into a CIGS absorber layer [20–22]. To date, the highest efficiency reported for a non-vacuum, solution-processed CIGS solar cell is approximately 17.3%, achieved using a hydrazine-based chalcogenide solution [20]. However, the high toxicity and handling risks associated with hydrazine have limited its scalability for industrial applications [21–24]. As a result, hydrazine-free solution routes have been developed as safer alternatives for fabricating CIGS absorbers [25–30]. Despite this progress, challenges such as complex synthesis procedures, limited ink stability, and suboptimal film crystallinity remain critical obstacles [26, 31, 32].

Recent studies have demonstrated the efficacy of thiol/amine mixtures in dissolving various metals and chalcogenide sources, facilitating the preparation of precursor solutions and the deposition of high-quality CIGS absorber layers [20, 26–34]. Photovoltaic devices using thiol/amine solutions have favourable CIGS absorber characteristics and have achieved device efficiencies of up to 13.12% [35–42]. Nonetheless, several outstanding issues pertaining to the selenization process require resolution, including (a) the formation of a fine-grained bottom layer, (b) a notable deviation in elemental composition, and (c) the formation of a thick $MoSe_2$ interlayer between Mo and CIGS layers post-selenization, all of which are generally regarded as detrimental to solar cell efficacy [36, 39].

It has been reported that post-selenization is an effective step to promote the crystal growth and to achieve the desired stoichiometry of the CIGS thin film and plays an important role in the microstructure and electrical properties of the CIGS absorber layer [16, 43] Selenization step usually requires sophisticated equipment and highly hazardous gaseous reactions with H_2Se or Se vapor, Moreover, during the post-selenization process, surface gas-phase reactions frequently lead to the formation of a double-layered structure in the absorber layer [30, 44].In the other hand, development of a solution-based approach for CIGS solar cells that does not require a post-deposition selenization step would thus result in improved reproducibility as well as significant cost reductions.

There have been interesting papers reporting selenization-free solution-based routes. Ray et al. [45] developed an environmentally friendly and low-cost method for CIGS films without selenization with toxic H_2Se or Se vapor. The relatively dense CIGS films were produced using infrared rapid thermal annealing (RTA) in an argon atmosphere at 500 °C, with a heating rate of 400 °C per minute. By quickly passing through the intermediate temperature range, the natural loss of selenium during heating was minimized. This process led to a clear improvement in the crystalline quality of the films, and their electrical measurements confirmed typical p-type semiconductor. Kuo et al. [46] also reported a similar process through which CIGS films were formed using particle-based screen printing followed by RTA sintering without additional Se. The organics are nearly entirely removed after 650 °C rapid annealing. Using normal loading during the annealing enhances film densification. stoichiometric chalcopyrite p-type CIGS film was successfully

prepared. Oh et al. [47] introduces a novel, simple, green fabrication route for CIGS films by spin coating of an aqueous precursor solution excluding the need for a complicated particle synthesis process and hazardous solvents. The process of selenization was successfully carried out with the incorporation of additional selenium solution. The CISSe thin-film solar cells achieved a maximum power conversion efficiency of 4.55% after being annealed at 550 °C. Despite the successful fabrication of phase-pure CIGS thin films with optimal composition, the solar cells produced from these films exhibit significantly lower performance compared to devices utilizing the conventional long-selenization process. Nonetheless, a comprehensive understanding of the primary efficiency-limiting factors in these selenization-free processes remains unclear.

Thiol–amine solvents systems offer the advantage of directly dissolving selenium precursors into the initial solution formulation [48, 49]. This capability enables the elimination of post-selenization processes, which typically involve complex equipment and hazardous gas-phase reactions. In such systems, a clean annealing process can be sufficient to produce high-quality absorbers by supplying an appropriate amount of selenium directly from the precursor solution [24, 26]. In this work, additional Se layers are introduced between the CIGS precursor layers by spin-coating a Se solution, leading to a multilayer absorber structure containing alternating CIGS and Se layers. This approach combines the advantages of thiol–amine solution chemistry with controlled selenium incorporation through spin-coated Se interlayers, providing a new pathway for selenization-free fabrication of CIGS absorbers. The effect of introducing Se during the coating process on the structural, compositional, and photovoltaic properties of the CIGS absorber layer is systematically investigated and compared with conventional selenization-based approaches.

2 Experimental section

Materials Copper(II) acetylacetonate ($Cu(acac)_2$, 99.9%), gallium(III) acetylacetonate ($Ga(acac)_3$, 99.99%), indium(III) acetate ($In(OAc)_3$, 99.9%), selenium pellets (Se, 99.99%), selenium powder (Se, 99.99%), 1,2-ethanedithiol ($C_2H_6S_2$, 95%), and 1,2-ethylenediamine ($C_2H_8N_2$, 99%).

Formation of precursor solution Two separate solutions were prepared: CIGS and Se solutions. CIGS ink was prepared by dissolving suitable quantities of Cu(acac)2, In(OAc)3, Ga(acac)3, and Se powder in a mixture of 1:10 v/v mixture of ethanedithiol (EDT) and ethylenediamine (en). The total concentration of the precursors was 0.2 M, and the molar ratio of Cu: In: Ga: Se was 0.9:0.7:0.3:2. The CIGS ink was stirred at 70 °C overnight until a homogeneous dark brown ink was obtained. The Se solution was prepared by dissolving Se powder in a mixture of 1:10 v/v (EDT)/(en) with a targeted concentration of 0.4 M. After the Se solution was stirred for a few hours at room temperature, the solution converted to a red transparent solution. All of the solution preparation processes were performed in an N_2-filled glovebox. A digital photograph of the prepared solutions is shown in Fig. 1.

Production of CIGS thin films CIGS precursor films were deposited onto 4 cm^2 molybdenum (Mo)-coated soda-lime glass (SLG) substrates using a spin-coating process and were subsequently converted into crystalline CIGS absorber layers during the rapid thermal annealing step. The CIGS ink was applied at 100 rpm for 5 s, followed by 3000 rpm for 30 s, and the deposition cycle was repeated eight times to form the absorber layer. To fabricate multilayered structures, selenium (Se) ink was intermittently spin-coated between the CIGS layers, introducing additional Se layers within the absorber. The number of Se insertions was controlled by adjusting the deposition sequence, resulting in different configurations denoted as 8-CIGS (no Se interlayers), 3Se/8CIGS (three Se layers), and 7Se/8CIGS (seven Se layers), as illustrated in Fig. 2. After each coating step, the films were annealed on a hot plate to remove organic components, with drying temperatures set to 300 °C for CIGS layers and 210 °C for Se layers, each for 2 min. These drying temperatures were selected based on preliminary optimization and previous reports on thiol–amine precursor

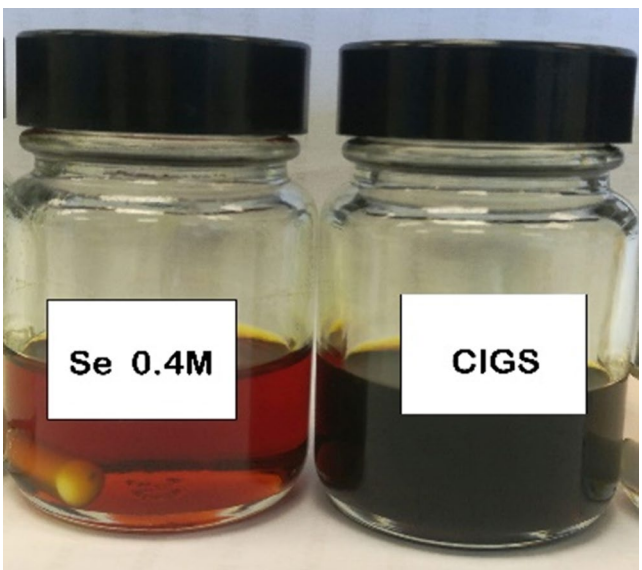

Fig. 1 Digital photographs for the CIGS and Se solutions

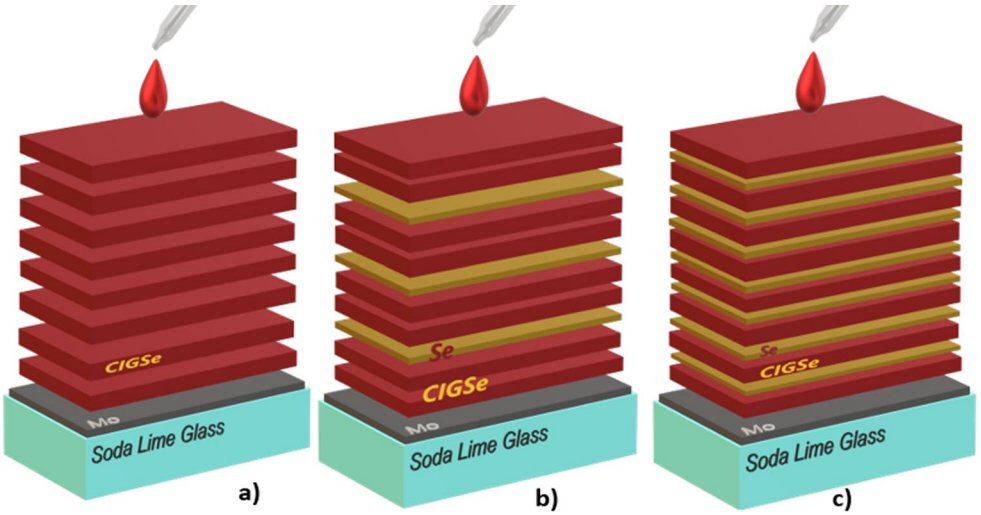

Fig. 2 Schematic illustration of the multilayer deposition sequence used to fabricate the CIGS absorber layers. The diagram shows the sequential spin-coating of CIGS precursor layers and intermediate Se layers, resulting in structures denoted as (a) 8CIGS (8 CIGS layers and no Se interlayers), (**b**) 3Se/8CIGS (8 CIGS layers and three Se interlayers), and (**c**) 7Se/8CIGS (8 CIGS layers and seven Se interlayers)

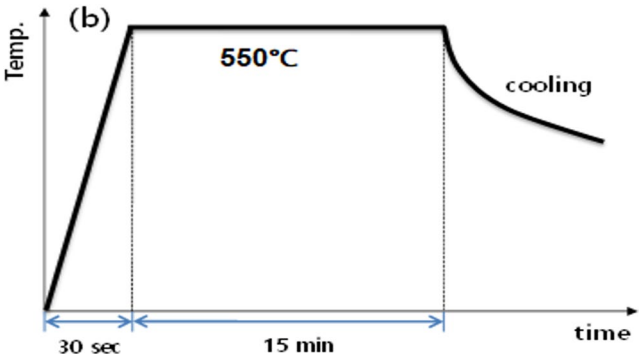

Fig. 3 Temperature profile used in this work

systems, where similar temperatures are used to promote solvent evaporation and partial precursor decomposition prior to high-temperature annealing.

Rapid thermal annealing After deposition, the films were annealed in a Rapid Thermal Processing (RTP) oven under nitrogen flow. The RTP oven used in this study was a MILA-5000 Ulvac-Riko system with infrared heating, which enabled extremely rapid heating. The samples were placed on a quartz holder next to a thermocouple, and heating was provided by four halogen lamps surrounding the sample. Upon loading the samples, a base pressure of 1×10^{-6} torr was achieved. Nitrogen gas was then introduced into the chamber to establish a pressure of 40 torr.

The precursor films were annealed in a nitrogen atmosphere without an additional selenium source. To prevent selenium depletion during the high-temperature process, the gas inlet and outlet were sealed during annealing. Figure 3 illustrates the temperature profile: the samples were rapidly heated to 550 °C within 30 s and maintained at this temperature for 15 min, followed by natural cooling to room temperature. The rapid heating to 550 °C promotes crystallization of the CIGS absorber layer and facilitates selenium diffusion within the multilayer stack, which enhances grain growth and improves phase formation.

Device fabrication CIGS thin-film solar cells were fabricated using a conventional heterojunction structure of SLG/Mo/CIGS/CdS/i-ZnO/Al: ZnO. The CIGS absorber layers prepared in this work were deposited on Mo-coated soda-lime glass (SLG) substrates, where the molybdenum layer (~500 nm) served as the back contact. The CIGS absorber layer was prepared following the procedure described in the previous section, which represents the primary variable investigated in this study. For structural and compositional characterization (SEM, XRD, and EDX), the CIGS films were deposited on bare soda-lime glass (SLG) substrates to avoid interference from the molybdenum back-contact layer. Mo-coated SLG substrates were used only for photovoltaic device fabrication.

A typical solar cell structure of SLG/Mo/CIGSe/CdS/i-ZnO/Al: ZnO was fabricated without any antireflection layer. A CdS buffer layer (~ 80 nm) was subsequently deposited by chemical bath deposition (CBD), followed by the deposition of intrinsic ZnO (i-ZnO, ~ 100 nm) and Al-doped ZnO (Al: ZnO, ~ 300 nm) window layers using RF magnetron sputtering. The photovoltaic performance of the devices was evaluated by current–voltage (J–V) measurements under AM 1.5G illumination (100 mW cm^{-2}, 25 °C) using a solar simulator. The key device parameters, including short-circuit current density (Jsc), open-circuit voltage (Voc), fill factor (FF), and power conversion efficiency (η), were extracted from the measured J–V curves [50–52]. Three independent devices were fabricated and measured for each condition to ensure statistical reproducibility of the photovoltaic results.

Characterization of CIGS thin films The structure of the produced films was studied using X-ray diffraction (XRD). The surface and cross-sectional morphologies of CIGS samples were examined using scanning electron microscopy (SEM). The SEM images were further processed using MountainsMap® surface analysis software (Digital Surf, France) for quantitative topography analysis [53]. The composition of CIGS thin films was examined using energy-dispersive X-ray spectroscopy (EDX). The optical characteristics were assessed using a UV–Vis–NIR spectrophotometer. J–V characteristics were measured under standard AM 1.5 illumination (100 mW/cm², 25 °C) using a solar simulator. Parameters including short-circuit current density (Jsc), open-circuit voltage (Voc), fill factor (FF), and power conversion efficiency (η) were calculated.

3 Results and discussion

The surface and cross-sectional morphology of annealed films with varying selenium (Se) interlayers between the CIGS layers were systematically characterized using scanning electron microscopy (SEM). The obtained images (Fig. 4a: top view; Fig. 4b: cross-section) were digitally enhanced and analyzed using MountainsMap software to quantify grain structure and film thickness.

A strong correlation was observed between the number of selenium layers and the resulting film structure. The 8CIGS–No Se sample, without additional Se layers, exhibited small and poorly fused grains with an average grain area of 0.063 µm², irregular grain boundaries, and a rough surface morphology with randomly distributed voids. The film thickness ranged between 0.5945 and 0.6577 µm. Together with the SEM observations of small, poorly fused grains and the broader XRD peak of the selenium-free sample, these results suggest limited grain growth and lower crystallinity. This observation is consistent with previous reports indicating that selenium acts as a catalyst during annealing, promoting grain growth and recrystallization [54]. The controlled addition of selenium resulted in a progressively denser absorber microstructure with larger and well-fused grains. The 3Se/8CIGS sample exhibited a thickness ranging from 0.7905 to 0.8355 µm and slightly larger grains (0.065 µm²), indicating that partial selenium incorporation promotes grain coalescence. The 7Se/8CIGS sample exhibited the most favourable microstructure, with a thickness ranging from 0.7522 to 0.8614 µm and prominent columnar grains (0.067 µm²). This trend confirms that sufficient selenium availability is crucial for optimal crystal growth, further supported by the increasing Se/(S + Se) ratio (0.28 to 0.58, Table 2) evaluated using EDX spectroscopy.

Additional insights were obtained from 3D surface topography analysis (Fig. 4c). The No-Se sample exhibited significant surface roughness characterized by a pronounced spiky texture, whereas the 7Se/8CIGS sample displayed a smoother and more uniform surface. This improvement arises from enhanced grain coalescence and reduced void formation during annealing. A substantial decrease in surface roughness is beneficial for solar applications, as it promotes grain coalescence, minimizes void formation during selenization, and reduces carrier recombination losses by providing smoother surfaces [51, 55].

Conventional solution-processed CISSe absorbers depend on gas-phase selenization, leading to a dual-layered structure characterized by a coarse upper layer and a fine-grained lower layer [56]. This structural inhomogeneity occurs due to the selenization process advancing from the surface inward, where the upper layer crystallizes first and subsequently serves as a diffusion barrier, restricting further reaction at the lower layers.

Our solution-phase selenization approach produces a homogeneous single-layer structure, thereby eliminating interfacial defects commonly found in conventional methods. The structural uniformity is anticipated to improve charge transport properties, rendering it especially beneficial for high-performance solar cell applications.

The surface composition of the CIGS absorbers was analyzed using energy-dispersive X-ray spectroscopy (EDX), which included point analysis for localized elemental quantification. Elemental ratios were calculated by averaging measurements obtained from three randomly selected points within each sample, as detailed in Table 1. The Se/(Se + S) ratio increased from 0.28 to 0.58 with the increasing number of Se ink deposition layers, indicating successful selenium incorporation into the absorber. Films that included three and seven intermediate Se layers (3Se/8CIGS and 7Se/8CIGS) demonstrated notably improved Se/(Se + S) ratios of 0.56 and 0.58, respectively. This trend aligns with previous studies indicating that incremental selenium loading through solution processing promotes uniform anion incorporation during annealing [54, 57].

The Cu/In ratio rose from 1.06 to 1.25 with increasing Se deposition. This trend may indicate enhanced Cu redistribution during annealing, possibly facilitated by the presence of selenium. However, further characterization techniques such as depth profiling or elemental mapping would be required to conclusively confirm Cu diffusion behavior. Enhanced copper inclusion could augment the electrical conductivity of the absorber by elevating hole carrier concentration and enhancing grain connectivity, contingent upon maintaining the composition within the ideal Cu-rich range (Cu/(In + Ga) = 0.9–1.2) [58–60]. Exceeding the threshold (Cu/(In + Ga) > 1.2–1.3) may result in the emergence of secondary

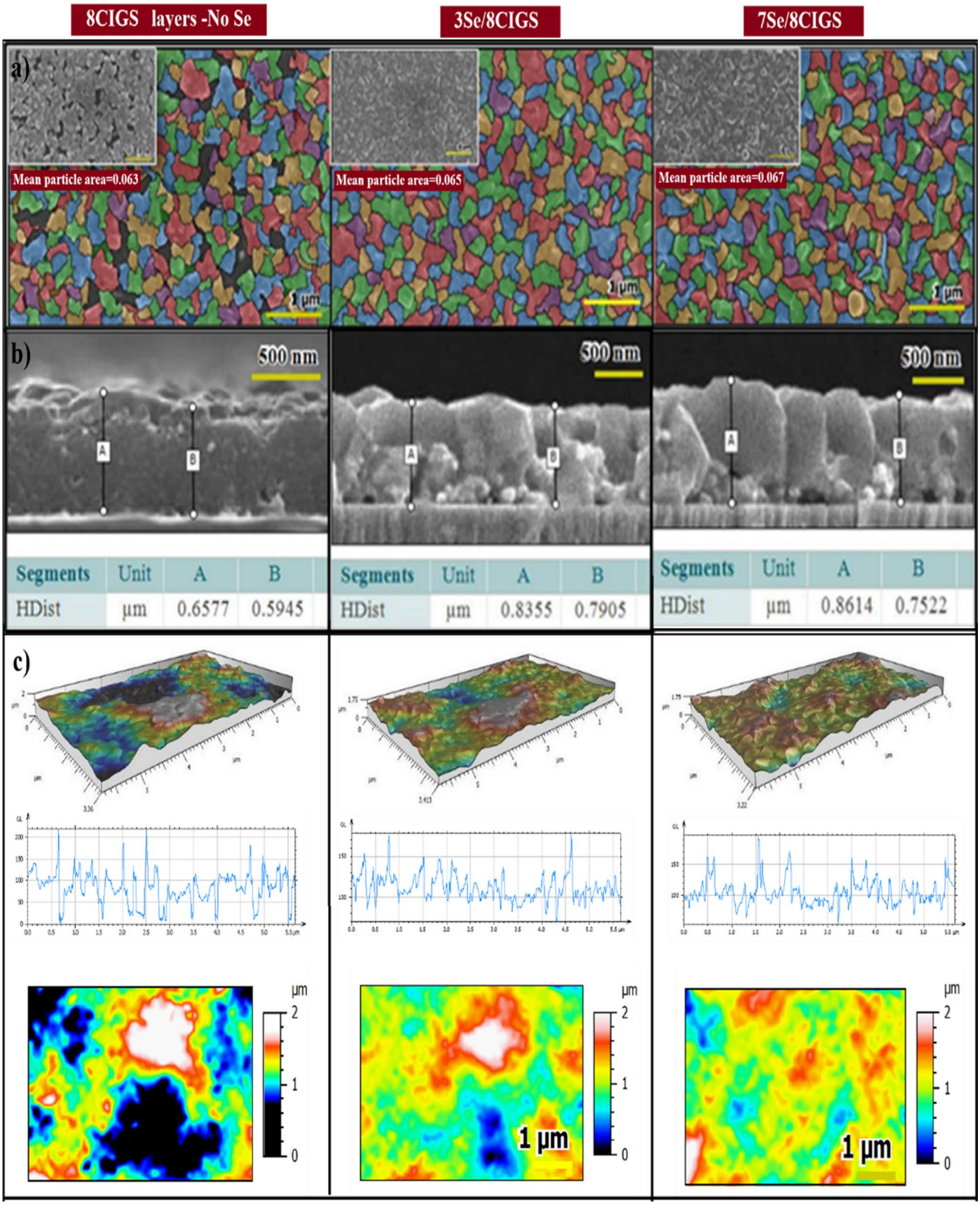
8CIGS layers -No Se
3Se/8CIGS
7Se/8CIGS
a)
Mean particle area=0.063
Mean particle area=0.065
Mean particle area=0.067
1 µm
b)
500 nm
A
B
Segments Unit A B
HDist µm 0.6577 0.5945
Segments Unit A B
HDist µm 0.8355 0.7905
Segments Unit A B
HDist µm 0.8614 0.7522
c)
µm
2
1
0
1 µm

Fig. 4 SEM-based morphological analysis of CIGSe thin films deposited with different numbers of intermediate selenium (Se) layers. The samples are denoted as 8CIGSe–No Se, 3Se/8CIGSe, and 7Se/8CIGSe. (**a**) Top-view SEM images showing the surface morphology and grain structure of the films. (**b**) Cross-sectional SEM images illustrating the thickness and columnar microstructure of the absorber layers. (**c**) Three-dimensional (3D) surface topography reconstructions, corresponding line profiles, and 2D surface maps generated using MountainsMap®. The 3D topography images were generated from the same surface regions as the corresponding top-view SEM images shown in (a)

copper-rich phases such as Cu_2Se, which are recognized for introducing deep-level defects and impairing device performance [61, 62].

Nevertheless, numerous obstacles persist. Solution-processed films frequently exhibit compositional gradients, porosity, and diminished uniformity in crystallinity, which can negatively impact device performance. These constraints can be alleviated by employing optimal annealing profiles and enhanced ink formulations [57, 65, 66]. Notwithstanding these obstacles, the Se-ink-based deposition method exhibits significant promise for economical, large-scale production of CIGS solar cells, especially within the framework of roll-to-roll or flexible substrate technologies.

X-ray diffraction (XRD) analysis was conducted to assess the crystal structure and phase purity of the CIGS thin films. Figure 5 shows that all samples exhibit the characteristic diffraction peaks of the chalcopyrite CIGS phase corresponding to the (112), (220)/(204), and (312)/(116) planes, consistent with the standard ICDD PDF card No. 35-1102, confirming the formation of the chalcopyrite structure. A systematic shift of the main (112) peak toward lower 2θ angles was observed with increasing selenium content, indicating lattice expansion resulting from the substitution of smaller sulphur atoms with larger selenium atoms.

The sharpness of the XRD peaks, particularly the (112) reflection, is directly correlated with the film's crystallinity. Narrower peaks, characterized by a reduced full width at half maximum (FWHM), suggest increased crystallite sizes, decreased lattice strain, and improved long-range order. The full width at half maximum (FWHM) of the (112) peak reduced from 1.223° in the selenium-free sample (8CIGS–No Se) to 0.608° and 0.591° in the selenium-rich samples (3Se/8CIGS and 7Se/8CIGS), respectively.

The optical properties of the CIGS absorber layers were systematically analyzed using UV–Vis–NIR spectroscopy, as shown in inset Fig. 6. All samples exhibited significant absorption throughout the visible to near-infrared (NIR) spectrum, a defining characteristic of high-quality photovoltaic absorbers. The absorption onset exhibited a shift toward longer wavelengths (redshift) as selenium content increased. The observed redshift signifies a reduction in the optical bandgap, corroborated by Tauc plot analysis.

The direct bandgap energies were estimated by extrapolating the linear portions of the Tauc plots, $(\alpha h\nu)^2$ versus $(h\nu)$. The bandgap decreased progressively from 1.238 eV for 8CIGS–NO Se to 1.218 eV for 3Se/8CIGS and ultimately to 1.203 eV for 7Se/8CIGS. The efficient substitution of selenium for sulfur inside the anion sublattice of the chalcopyrite structure is indicated by the systematic decrease in bandgap, which is highly correlated with the increase in the Se/(S + Se) atomic ratio, as validated by EDX measurements.

Controlled selenium integration provides bandgap tunability, which is beneficial for improving the spectrum of solar absorption. A narrower bandgap increases the absorption edge, thereby enhancing photon harvesting in the near-infrared region and improving current generation in solar cells. Additionally, bandgap engineering in CIGS enhances spectral alignment with the solar spectrum and supports tandem cell applications when combined with higher-bandgap top cells. The findings confirm that the solution-based Se incorporation method effectively modifies the optical properties of CIGS films, indicating its potential for improving the efficiency of thin-film photovoltaic devices [65, 66].

Thin-film solar cells based on solution-processed CIGS were fabricated using the device architecture Mo/SLG/CIGS/CdS/i-ZnO/Al: ZnO, without an antireflection layer. For each experimental condition, multiple devices were fabricated and characterized to verify reproducibility. The photovoltaic parameters reported correspond to representative devices showing consistent performance trends. Figure 7; Table 3 summarize the best photovoltaic performance of the fabricated devices obtained from current density–voltage (J–V) measurements under standard AM 1.5G illumination. The reported values correspond to representative devices showing consistent performance trends across multiple fabricated devices.

The 7Se/8CIGS device exhibited the highest power conversion efficiency (PCE) of 5.13%, with an open-circuit voltage (Voc) of 382 mV, a short-circuit current density (Jsc) of 23.8 mA cm^{-2}, and a fill factor (FF) of 56.0%. The 3Se/8CIGS device achieved a comparable PCE of 5.03%, while the reference 8CIGS–No Se device showed a significantly lower efficiency of 3.15%, with a Voc of 318 mV and FF of 53.3%. These results demonstrate that the introduction of intermediate selenium layers significantly improves the photovoltaic performance of the devices.

A closer examination of the photovoltaic parameters provides further insight into the origin of this performance improvement. The short-circuit current density (Jsc) increased from 18.6 to approximately 24 mA cm^{-2}, which is consistent with the reduction in bandgap energy and the enhanced optical absorption in the near-infrared region resulting from increased selenium incorporation. The

Table 1 Chemical composition of the CIGS thin films deposited with varying numbers of Se interlayers between the CIGS

	In (at.%)	Cu (at.%)	Ga (at.%)	S (at.%)	Se (at.%)	Cu/In	Se/(S+Se)
8CIGS-NO Se	16.28	17.24	7.62	42.62	16.24	1.06	0.28
3Se/8CIGS	16.93	20.56	8.03	24.02	30.46	1.21	0.56
7Se/8CIGS	16.58	20.73	7.99	23.01	31.69	1.25	0.58

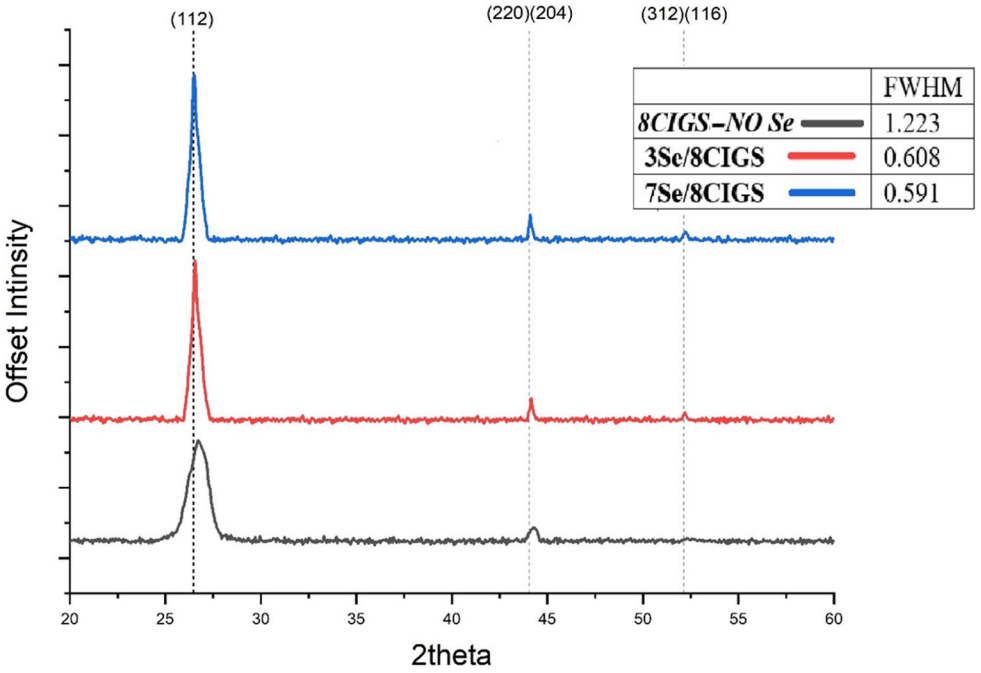

Fig. 5 X-ray diffraction (XRD) patterns and full-width at half-maximum (FWHM) of the (112) peaks from the XRD data of the CIGS thin films deposited with varying numbers of Se interlayers between the CIGS layers

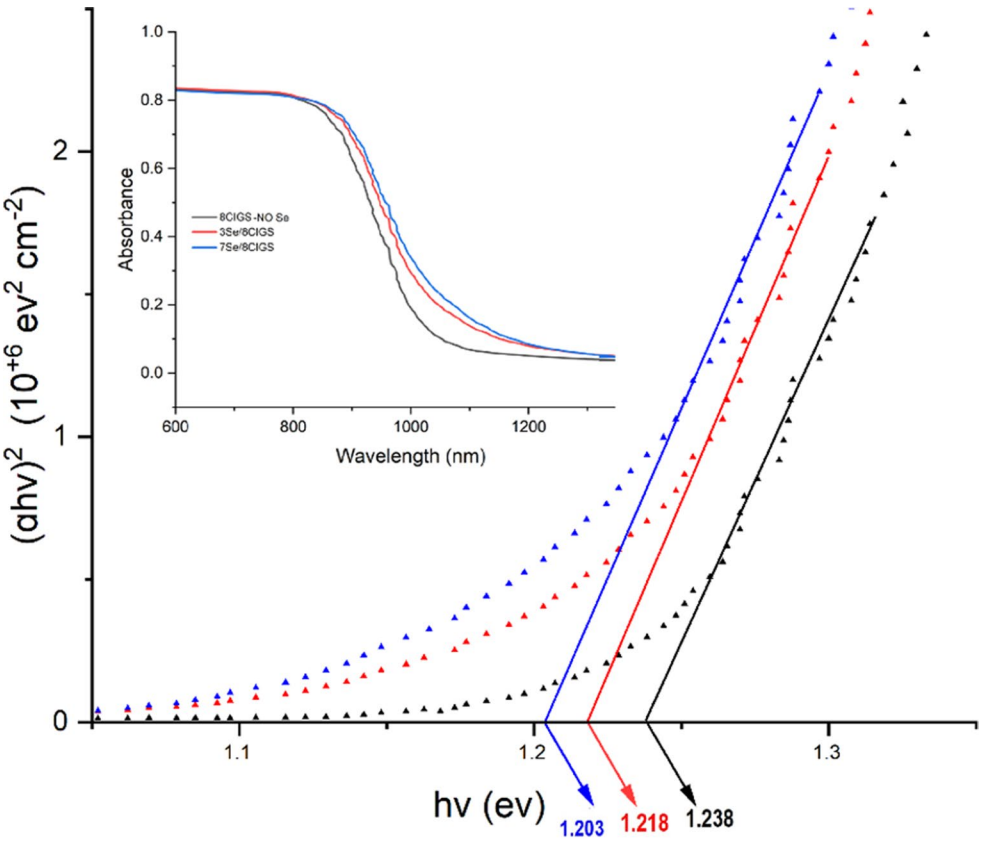

Fig. 6 Tauc plot for the calculation of optical band gap energy Inset show UV-Vis absorption spectra of CIGS thin films with varying numbers of intermediate selenium layers

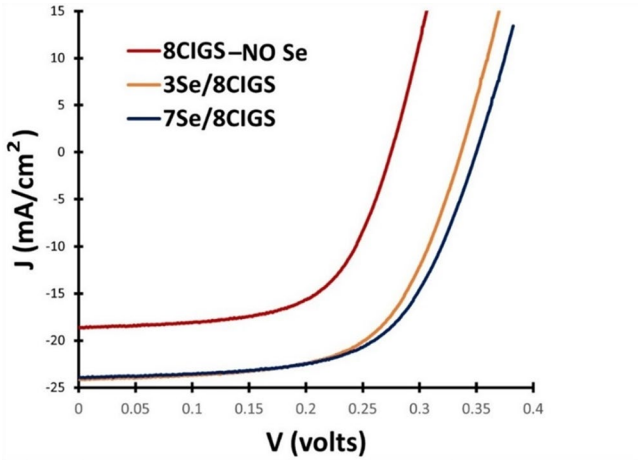

Fig. 7 Current density−voltage (J−V) characteristics of CIGS with varying numbers of intermediate selenium layers

Table 2 Device performance of CIGS solar cells prepared with varying numbers of intermediate selenium layers. The reported photovoltaic parameters correspond to representative devices fabricated under identical conditions

Sample	Eg (eV)	Voc (mV)	Jsc(mA/cm²)	FF (%)	η (%)
8CIGS–NO Se	**1.238**	**318**	**18.6**	**53.3**	**3.15**
3Se/8CIGS	**1.218**	**372**	**24.1**	**56.2**	**5.03**
7Se/8CIGS	**1.203**	**382**	**23.8**	**56.0**	**5.13**

improvement in the open-circuit voltage (Voc) can be attributed to enhanced absorber crystallinity and reduced recombination at grain boundaries, as suggested by the larger grain sizes observed in the SEM images and the reduced full width at half maximum (FWHM) of the XRD peaks. In addition, the moderate increase in the fill factor (FF) indicates improved charge transport and reduced series resistance within the absorber layer, which can be associated with the more compact and uniform microstructure obtained after introducing selenium interlayers.

Overall, the improvement in device performance with increasing selenium content is attributed to enhanced crystallinity, grain growth, and defect passivation within the absorber layer. The incorporation of selenium reduces the optical bandgap from 1.238 eV to 1.203 eV, (Table 2), which enhances light absorption and charge carrier generation, thereby increasing Jsc. Furthermore, improved crystal quality and reduced defect density help suppress recombination losses, leading to higher Voc and FF values in the selenium-modified devices, as supported by the SEM and XRD analyses. Although the efficiency increase from the 3Se/8CIGS to the 7Se/8CIGS device is relatively small, this behaviour suggests that further performance improvements may require additional optimization of absorber composition, defect density, and interface quality.

It should be noted that the power conversion efficiency obtained in this study (5.13%) remains lower than the current world-record efficiency of approximately 23–24% reported for vacuum-processed CIGS solar cells. However, these high-efficiency devices typically rely on sophisticated vacuum deposition techniques and long gas-phase selenization processes. In contrast, the present work focuses on a solution-processed and selenization-free fabrication route, which significantly simplifies the manufacturing process and reduces the use of hazardous gaseous selenium sources. Therefore, the achieved efficiency should be evaluated in the context of early-stage solution-processed CIGS devices, where efficiencies are generally lower but the potential for low-cost and scalable fabrication is significantly higher.

Both Se-incorporated samples (3Se/8CIGS and 7Se/8CIGS) exhibited comparable photovoltaic performance, indicating that a moderate introduction of selenium (as seen in 3Se/8CIGS) can significantly improve film quality and device efficiency. This underscores the strength of selenium-induced enhancements and indicates a potential performance plateau beyond which further selenium may yield diminishing returns.

4 Conclusion

This work presents a solution-based method for the fabrication of CIGS thin-film solar cells by introducing intermediate selenium layers within the CIGS layers, thereby eliminating the need for conventional selenization processes. The additional Se layers were deposited during the spin-coating process using a Se solution dissolved in thiol amine solvents. The incorporation of selenium during the deposition stage improved grain growth, crystallinity, selenium incorporation, and the overall quality of the absorber layer while eliminating the need for toxic H_2Se or Se vapor and complex vacuum-based equipment. The proposed method resulted in improved photovoltaic performance, with the 7Se/8CIGS device achieving a peak efficiency of 5.13%. These results demonstrate the potential of this cost-effective and scalable method for producing large-area and flexible CIGS photovoltaic devices.

Further optimization of annealing conditions and selenium incorporation may lead to additional improvements in device performance and support the future development of solution-processed CIGS solar cells. In contrast to traditional vacuum-based fabrication techniques followed by conventional selenization processes, the solution-based process employed in this work without any additional selenization step presents a cost-effective and scalable alternative with reduced equipment complexity. Vacuum-based techniques allow precise control of elemental fluxes and substrate temperature, enabling the fabrication of high-efficiency CIGS absorber layers with well-defined grain structures and

stoichiometry [63, 64]. However, such approaches are associated with high capital costs and limited throughput. The spin-coating of Se ink combined with solution-deposited CIGS precursors enables flexible adjustment of selenium content through a modular deposition sequence, offering a simplified route for absorber fabrication.

Acknowledgments The authors acknowledge the Institute of Nano Electronic Engineering, University Malaysia Perlis, for the support. Special thanks to those who contributed to this project directly or indirectly.

Author contributions G.B. conceptualized and designed the experiments, performed the solution processing and film fabrication, conducted characterization (SEM, EDX, XRD, optical), and wrote the manuscript. All authors read, reviewed, and approved the final manuscript.

Funding Open access funding provided by The Ministry of Higher Education Malaysia and Universiti Malaysia Perlis. This research received no specific grant from any funding agency in the public, commercial, or not-for-profit sectors.

Data availability The datasets generated and/or analysed during the current study are available from the corresponding author upon reasonable request.

Declarations

Ethics approval and consent to participate Not applicable. This study did not involve humans or animals.

Competing interests The authors declare that they have no competing interests.

References

1. T. Feurer, P. Reinhard, E. Avancini, B. Bissig, J. Löckinger, P. Fuchs, R. Carron, T.P. Weiss, J. Perrenoud, S. Stutterheim, S. Buecheler, A.N. Tiwari, Prog. Photovoltaics Res. Appl. **25**, 645 (2017)
2. J. Ramanujam, U.P. Singh, Energy Environ. Sci. **10**, 1306 (2017)
3. U.P. Singh, S.P. Patra, International Journal of Photoenergy 2010, 1 (2010)
4. J. Keller, K. Kiselman, O. Donzel-Gargand, N.M. Martin, M. Babucci, O. Lundberg, E. Wallin, L. Stolt, M. Edoff, Nat. Energy. **9**, 467 (2024)
5. P. Jackson, R. Wuerz, D. Hariskos, E. Lotter, W. Witte, M. Powalla, Phys. Status Solidi (RRL) - Rapid Res. Lett. **10**, 583 (2016)
6. P. Jackson, D. Hariskos, R. Wuerz, O. Kiowski, A. Bauer, T.M. Friedlmeier, M. Powalla, Phys. Status Solidi (RRL) – Rapid Res. Lett. **9**, 28 (2015)
7. M. Powalla, P. Jackson, W. Witte, D. Hariskos, S. Paetel, C. Tschamber, W. Wischmann, Sol Energy Mater. Sol Cells. **119**, 51 (2013)
8. M. Nakamura, K. Yamaguchi, Y. Kimoto, Y. Yasaki, T. Kato, H. Sugimoto, IEEE J. Photovolt. **9**, 1863 (2019)
9. J.C. Park, M. Al-Jassim, S.W. Shin, J.H. Kim, T.W. Kim, Ceram. Int. **45**, 4424 (2019)
10. D.G. Moon, J.H. Yun, J. Gwak, S. Ahn, A. Cho, K. Shin, K. Yoon, S. Ahn, Energy Environ. Sci. **5**, 9914 (2012)
11. C.H. Chen, W.C. Shih, C.Y. Chien, C.H. Hsu, Y.H. Wu, C.H. Lai, Sol. Energy Mater. Sol. Cells. **103**, 25 (2012)
12. X. Lyu, D. Zhuang, M. Zhao, N. Zhang, Y. Wei, Y. Wu, G. Ren, C. Wang, L. Hu, J. Wei, Q. Gong, Ceram. Int. **45**, 16405 (2019)
13. M. Green, E. Dunlop, J. Hohl-Ebinger, M. Yoshita, N. Kopidakis, X. Hao, Prog. Photovoltaics Res. Appl. **29**, 3 (2021)
14. C.J. Hibberd, E. Chassaing, W. Liu, D.B. Mitzi, D. Lincot, A.N. Tiwari, Prog. Photovoltaics Res. Appl. **18**, 434 (2010)
15. D. Lee, K. Yong, Korean J. Chem. Eng. **30**, 1347 (2013)
16. S. Ahn, C. Kim, J.H. Yun, J. Gwak, S. Jeong, B.H. Ryu, K. Yoon, J. Phys. Chem. C **114**, 8108 (2010)
17. A. Cho, S. Ahn, J.H. Yun, J. Gwak, H. Song, K. Yoon, J. Mater. Chem. **22**, 17893 (2012)
18. S. Ahn, K.-H. Kim, J.-H. Yun, K.-H. Yoon, J. Appl. Phys. **105, (2009)**
19. S.M. McLeod, C.J. Hages, N.J. Carter, R. Agrawal, Prog. Photovoltaics Res. Appl. **23**, 1550 (2015)
20. T. Zhang, Y. Yang, D. Liu, S.C. Tse, W. Cao, Z. Feng, S. Chen, L. Qian, Energy Environ. Sci. **9**, 3674 (2016)
21. A.R. Katritzky, J. Am. Chem. Soc. **124**, 6504 (2002)
22. B. Bob, B. Lei, C.H. Chung, W. Yang, W.C. Hsu, H.S. Duan, W.W.J. Hou, S.H. Li, Y. Yang, Adv. Energy Mater. **2**, 504 (2012)
23. E. Schmidt, Hydrazine and Its Derivatives: Preparation, Properties, Applications, Second (Wiley-Interscience) (2001)
24. G. Regmi, A. Ashok, P. Chawla, P. Semalti, S. Velumani, S.N. Sharma, H. Castaneda, J. Mater. Sci.: Mater. Electron. **31**, 7286 (2020)
25. S. Suresh, A.R. Uhl, Adv. Energy Mater. **11**, 2003743 (2021)
26. B. Kim, B.K. Min, Sustain. Energy Fuels. **2**, 1671 (2018)
27. S.K. Karunakaran, G.M. Arumugam, W. Yang, S. Ge, S.N. Khan, X. Lin, G. Yang, J. Mater. Chem. Mater. **7**, 13873 (2019)
28. A.R. Uhl, J.K. Katahara, H.W. Hillhouse, Energy Environ. Sci. **9**, 130 (2016)
29. Y. Xie, H. Chen, A. Li, X. Zhu, L. Zhang, M. Qin, Y. Wang, Y. Liu, F. Huang, J. Mater. Chem. Mater. **2**, 13237 (2014)
30. G. Wang, S. Wang, Y. Cui, D. Pan, Chem. Mater. **24**, 3993 (2012)
31. A.R. Uhl, C. Fella, A. Chirilă, M.R. Kaelin, L. Karvonen, A. Weidenkaff, C.N. Borca, D. Grolimund, Y.E. Romanyuk, A.N. Tiwari, Prog. Photovoltaics Res. Appl. **20**, 526 (2012)
32. S.J. Park, Y. Cho, S.H. Moon, J.E. Kim, D.K. Lee, J. Gwak, J. Kim, D.W. Kim, B.K. Min, J. Phys. D Appl. Phys. **47**, 305 (2014)
33. T.K. Todorov, O. Gunawan, T. Gokmen, D.B. Mitzi, Prog. Photovoltaics Res. Appl. **21**, 82 (2013)
34. L. Yalçin, R. Öztürk, J. Optoelectron. Adv. Mater. **15**, 326 (2013)
35. D. Zhao, Q. Tian, Z. Zhou, G. Wang, Y. Meng, D. Kou, W. Zhou, D. Pan, S. Wu, J. Mater. Chem. Mater. **3**, 19263 (2015)
36. D. Zhao, Q. Fan, Q. Tian, Z. Zhou, Y. Meng, D. Kou, W. Zhou, S. Wu, J. Mater. Chem. A **4**, 13476 (2016)

37. M. Zhao, M.J. Xin Lu, Koeper, R. Agrawal, J. Mater. Chem. A **4**, 7390 (2016)
38. P. Arnou, M.F.A.M. van Hest, C.S. Cooper, A.V. Malkov, J.M. Walls, J.W. Bowers, ACS Appl. Mater. Interfaces. **8**, 11893 (2016)
39. P. Arnou, C.S. Cooper, S. Uličná, A. Abbas, A. Eeles, L.D. Wright, A.V. Malkov, J.M. Walls, J.W. Bowers, Thin Solid Films. **633**, 76 (2017)
40. Q. Fan, Q. Tian, H. Wang, F. Zhao, J. Kong, S. Wu, J. Mater. Chem. Mater. **6**, 4095 (2018)
41. S. Uličná, P. Arnou, A. Abbas, M. Togay, L.M. Welch, M. Bliss, A.V. Malkov, J.M. Walls, J.W. Bowers, J. Mater. Chem. Mater. **7**, 7042 (2019)
42. G. Albalawneh, M. Ramli, ECS J. Solid State Sci. Technol. **9**, 061013 (2020)
43. A.E. Zaghi, M. Buffière, J. Koo, G. Brammertz, M. Batuk, C. Verbist, J. Hadermann, W.K. Kim, M. Meuris, J. Poortmans, J. Vleugels, Thin Solid Films. **556**, 20 (2014)
44. J.M. Raguse, C.P. Muzzillo, J.R. Sites, L. Mansfield, IEEE J. Photovolt. **7**, 303 (2017)
45. J. Ray, C. Desai, B. Panchal, Rehani, and P. K. Mehta, Undefined (2013)
46. H.P. Kuo, H.A. Tsai, A.N. Huang, W.C. Pan, Appl. Energy. **164**, 1003 (2016)
47. Y. Oh, W. Yang, J. Kim, K. Woo, J. Moon, ACS Appl. Mater. Interfaces. **7**, 22570 (2015)
48. D.H. Webber, R.L. Brutchey, J. Am. Chem. Soc. **135**, 15722 (2013)
49. D.H. Webber, J.J. Buckley, P.D. Antunez, R.L. Brutchey, Chem. Sci. **5**, 2498 (2014)
50. S. Rehan, K.Y. Kim, J. Han, Y.J. Eo, J. Gwak, S.K. Ahn, J.H. Yun, K.H. Yoon, A. Cho, S.J. Ahn, ACS Appl. Mater. Interfaces. **8**, 5261 (2016)
51. J.H. Han, S. Rehan, D.G. Moon, A. Cho, J. Gwak, K.H. Yoon, S.K. Ahn, J.H. Yun, Y.J. Eo, S. Ahn, J. Mater. Chem. Mater. **4**, 6319 (2016)
52. M.A. Contreras, M.J. Romero, B. To, F. Hasoon, R. Noufi, S. Ward, K. Ramanathan, Thin Solid Films. **403–404**, 204 (2002)
53. Digital Surf, MountainsMap® Surface analysis software; Digital surf: Besançon, France
54. W. Septina, M. Kurihara, S. Ikeda, Y. Nakajima, T. Hirano, Y. Kawasaki, T. Harada, M. Matsumura, ACS Appl. Mater. Interfaces. **7**, 6472 (2015)
55. Z. Cevher, Optimization of CuInxGa1–xSe2 Solar Cells with Post Selenization, PhD Thesis, City University of New York (CUNY) 2018
56. G.M. Albalawneh, M.M. Ramli, M.Z.M. Zain, Z. Sauli, J Phys Conf Ser 2053, (2021)
57. T. Zhang, Y. Yang, D. Liu, S.C. Tse, W. Cao, Z. Feng, S. Chen, L. Qian, Energy Environ. Sci. **9**, 3874 (2017)
58. J. Yan, J.K. Nørskov, Phys. Rev. B Condens. Matter Mater. Phys. **88**, 245204 (2013)
59. S.C. Chen, S.W. Wang, S.Y. Kuo, J.Y. Juang, P.T. Lee, C.W. Luo, K.H. Wu, H.C. Kuo, Nanoscale Res. Lett. **12 (2017)**
60. J. Wang, Y.F. Zhang, J. Zhu, Adv. Mat. Res. **815**, 448 (2013)
61. J.T. Heath, J.D. Cohen, W.N. Shafarman, D.X. Liao, A.A. Rockett, Appl. Phys. Lett. **80**, 4540 (2002)
62. S. Niki, M. Contreras, I. Repins, M. Powalla, K. Kushiya, S. Ishizuka, K. Matsubara, Prog. Photovoltaics Res. Appl. **18**, 453 (2010)
63. M.A. Contreras, M.J. Romero, R. Noufi, Thin Solid Films. **511**, 51 (2006)
64. R. Kaigawa, K. Ban, S. Merdes, T. Dittrich, R. Klenk, in Energy Procedia (2011), pp. 297–302
65. M. Gloeckler, J.R. Sites, J. Phys. Chem. Solids. **66**, 1891–1894 (2005)
66. J.F. Guillemoles, J.P. Connolly, O. Ramdani, O. Roussel, D. Guimard, V. Bermudez, N. Naghavi, P.P. Grand, L. Parissi, J. Kurdi, J. Kessler, O. Kerrec, D. Lincot, J. Nano Res. **4**, 79 (2008)